Acta Geochim (2022) 41(2):226–243
https://doi.org/10.1007/s11631-021-00511-0

ORIGINAL ARTICLE

Trace element and sulfur isotope compositions of pyrite from the Tianqiao Zn–Pb–Ag deposit in Guizhou province, SW China: implication for the origin of ore-forming fluids

Yumiao Meng[1] · Xiaowen Huang[1] · Chunxia Xu[2] · Songning Meng[1,3]

Received: 24 September 2021 / Revised: 2 November 2021 / Accepted: 3 November 2021 / Published online: 6 January 2022

Abstract The Tianqiao Zn–Pb–Ag deposit in SW China, hosted by Devonian and Carboniferous limestone and clay rocks, is composed of sulfides such as sphalerite, galena, and pyrite. Pyrite is present in different paragenetic stages and can be divided into four types based on textures and mineral assemblages. Pyrite from the adjacent Shanshulin deposit (Py-SSL) is also used for comparison. Py1 shows framboid texture with grain diameter up to 1 mm and was commonly replaced by sphalerite. Py2 is characterized by overgrowth texture and displays inner oscillatory zoning. Py2 is associated with abundant sphalerite and galena. Py3 shows replacement relics textures where galena fills the fractures of pyrite. Py4 is a euhedral to subhedral crystal disseminated in dolomite and is characterized by deformation and fragmentation textures. Minor sphalerite and galena are associated with Py4. Py-SSL is subhedral and disseminated in dolomite, similar to Py4. Py1 was formed by a diagenetic or sedimentary process, whereas Py2 and Py3 were formed by multiple stages of ore fluids. Py4 and Py-SSL were formed at the carbonate-sulfide stage, but Py4 suffered from deformation after its formation. Py1, Py2, and Py3 are characterized by relative enrichment of Sb, Cu, and As, in contrast to Py4 and Py-SSL with higher Cr, W, Ge, Sn, Tl, Ni, and Ga contents. However, critical metals such as Ge, Ga, and In in pyrite are generally lower than 10 ppm, which are not economically important. The trace element variation in Tianqiao pyrite with paragenesis results from fluid evolution in the Pb–Zn ore system and competition with co-precipitating minerals. Diagenetic and ore-forming hydrothermal fluids are responsible for the formation of different types of pyrite. Ore-related pyrite from the Tianqiao and Shanshulin deposits has Co and Ni distribution features similar to pyrite from sedimentary pyrite and submarine hydrothermal vents, different from those in volcanogenic massive sulfide, iron oxide-copper–gold, and porphyry Cu deposits, indicating their derivation of relatively low-temperature (< ~ 250 °C) hydrothermal fluids, similar to basin brines or seawater., via fluid-rock interaction. This conclusion is also supported by the sulfur isotope composition of sulfides which are 13.0–13.5 ‰, and 15.6–20.5 ‰ for Tianqiao and Shanshulin deposits, respectively.

Keywords Trace elements · Pyrite · Sulfur isotopes · Tianqiao and Shanshulin Zn–Pb–Ag · Origin of ore-forming fluids

✉ Chunxia Xu
xuchunxia_nit@163.com

Yumiao Meng
mengyumiao@mail.gyig.ac.cn

Xiaowen Huang
huangxiaowen@mail.gyig.ac.cn

Songning Meng
2797178763@qq.com

[1] State Key Laboratory of Ore Deposit Geochemistry, Institute of Geochemistry, Chinese Academy of Sciences, Guiyang 550081, China

[2] School of Hydraulic and Ecological Engineering, Nanchang Institute of Technology, Nanchang 330099, China

[3] Applied Nuclear Technology in Geosciences Key Laboratory of Sichuan Province, Chengdu University of Technology, Chengdu 610059, Sichuan, China

1 Introduction

The Sichuan-Yunnan-Guizhou (SYG) Pb–Zn metallogenic belt, located in the western Yangtze Block (Fig. 1a), is one of the largest Pb–Zn producers in the world. The belt comprises over 400 Pb–Zn deposits and has Pb–Zn ore resources of more than 200 million tons (Mt) @ 5 wt% Pb and 10 wt% Zn (Fig. 1b) (Han et al. 2007; Zhou et al. 2013; Bao et al. 2017; Hu et al. 2017; Zhang et al. 2019; Li et al. 2020). These Pb–Zn deposits are hosted in Sinian (Ediacaran) to Permian carbonate rocks and are controlled by thrust fault-fold structures, which are spatially related to pervasive Permian Emeishan flood basalts (Fig. 1b) (Liu and Lin 1999; Han et al. 2007).

The Tianqiao medium-size Pb–Zn deposit along the Yadu–Mangdong fault has been mined for over past decades (Mao et al. 2001; Jin 2008). Numerous studies of this deposit include geology, geochronology, and geochemistry (Mao et al. 2001; Jin 2008; Zhou et al. 2013, 2014; Li et al. 2016). Jin (2008) and Mao et al. (2001) considered that the Tianqiao deposit can represent all the Pb–Zn deposits in the Guizhou area of SYG based on geological features. According to the ages and origin of the ore-forming metals, it is generally considered to be a sediment-reworked deposit related to the host carbonate rocks and the thrust-fold structure and is an example of Mississippi Valley-type (MVT) Zn–Pb deposits (Zhang et al. 2015; Li et al. 2016; Hu et al. 2017). For a specific deposit type, the origin of ore-forming fluids will be diverse from one deposit to another. Therefore, the origin of the Tianqiao deposit is further evaluated here using pervasive pyrite in Pb–Zn deposits.

A series of trace elements are present in pyrite as lattice substitution or nanoinclusions (Huston et al. 1995; Abraitis et al. 2004; Large et al. 2009; Reich et al. 2013; Deditius et al. 2014; Cook et al. 2016). Pyrite is a good indicator mineral for ore genesis research (Cook et al. 2009, 2016; Reich et al. 2013, 2016; Gregory et al. 2016; Tanner et al.

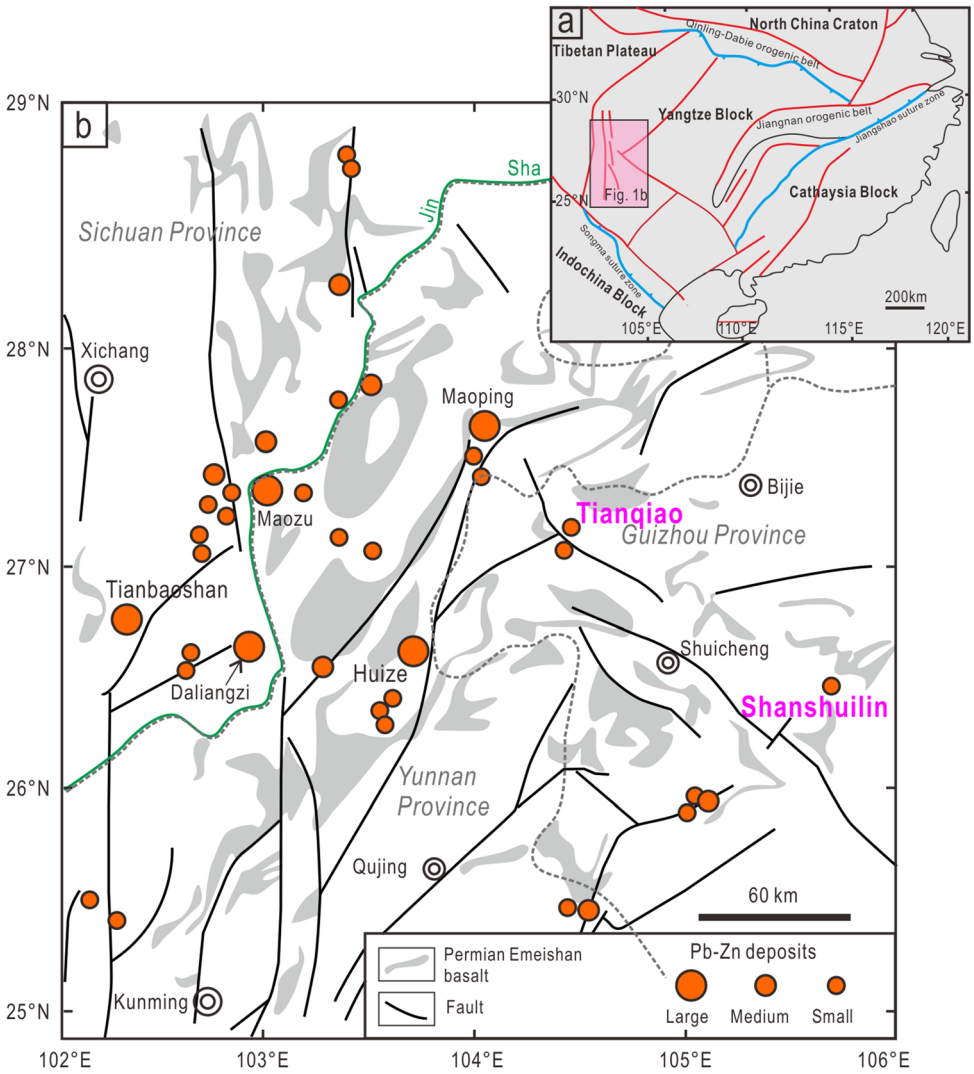

Fig. 1 **a** A simplified geological map showing the location of the study area in the Yangtze Block (modified from Hu et al. 2017). **b** A map showing the location of Tianqiao and Shanshuilin deposits in the Sichuan-Yunan-Guizhou Pb–Zn metallogenic belt (modified from Han et al. 2007 and Hu et al. 2017)

2016; Ward et al. 2017; Meng et al. (2018, 2019) and mineral exploration (Baker et al. 2006; Franchini et al. 2015; Mukherjee and Large 2017). Pyrite occurs in the whole paragenetic stages of the Tianqiao Pb–Zn deposit, and thus records the variation of fluids evolving from barren to mineralization.

In this study, mineralogy and detailed textures of pyrite from the Tianqiao deposit were characterized by optical microscope and back-scattered imaging in electronic microprobe. Four types of pyrite are defined based on textures and mineral assemblages. Pyrite from the adjacent Shanshulin deposit is also studied for comparison. Trace elements in pyrite were determined by laser ablation inductively coupled plasma mass spectrometry (LA-ICP-MS), and investigated by principal component analysis to highlight the chemical variation of different pyrite types. In combination with sulfur isotopes of sulfides, the trace element data was used to unravel the origin of pyrite and thus the ore-forming fluids.

2 Geological background

2.1 Regional geology

The Yangtze Block is separated from other blocks by a series of orogenic belts and suture zones. In the north, the Triassic Qinling–Dabie orogenic belt separates the Yangtze Block from the North China Craton, whereas in the southeast the Jiangshao Neoproterozoic suture zone ($\sim$ 830 Ma) marks the boundary between the Yangtze Block and the Cathaysia Block (Zhou et al. 2008; Zhao et al. 2011) (Fig. 1a). In the southwest, the Yangtze Block is separated from the Indochina Block by the Songma suture zone (Fig. 1a). The Yangtze Block is composed of a Late Archean basement covered by Neoproterozoic to Cenozoic sedimentary rocks of shallow marine origin (Zhou et al. 2002; Yan et al. 2003). The crystalline basement is different in the northern and western part of the Yangtze Block, which consists of $\sim$ 2.9 to 3.3 Ga tonalite-trondhjemite-granodiorite (TTG) and metamorphic rocks in the north (Qiu et al. 2000; Gao et al. 2011), and $\sim$ 1.7 Ga Dongchuan and $\sim$ 1.0 Ga Huili Groups in the west (Sun et al. 2009; Zhao et al. 2011).

In the western Yangtze Block, Permian Emeishan flood basalts are widespread, which is possibly related to $\sim$ 260 Ma mantle plume activity (Fig. 1b) (Chung and Jahn 1995; Zhou et al. 2002). The flood basalts and interlayered Permian limestone constitute the Emeishan Large Igneous Province (ELIP). There are also some mafic–ultramafic intrusions in ELIP where magmatic sulfide or oxide deposits are present (Zhou et al. 2008). Over 400 Pb–Zn deposits in the western Yangtze Block are distributed in a limited area which is called as SYG Pb–Zn metallogenic belt (Fig. 1b) (Liu and Lin 1999). These Pb–Zn deposits are composed of irregular ore bodies with simple mineralogy, weakly wall rock alteration, high contents of Zn + Pb, and economically important Ag, Ge, Cd, Ga, and In (Liu and Lin 1999). These deposits show a close spatial relationship with Permian Emeishan basalts.

2.2 Deposit geology

The Tianqiao Zn–Pb–Ag deposit in the Guizhou province, an important component of the SYG metallogenic belt, contains about 0.38 million tons Pb and Zn metals grading $>$ 15 % Pb + Zn (Zhou et al. 2013). Other economical elements such as Ge, Ga, Cd, and Ag are also present in some ores with sphalerite and galena as main host minerals (Zhou et al. 2011). Major ore bodies, including Shazidi, Yingpanshang, and Haozidong, are hosted in Devonian and Carboniferous limestone and clay rocks and are controlled by a thrust fault and anticline (Fig. 2). Diabase dykes are also locally present along the fault.

Oxidized Pb–Zn ores of the Tianqiao deposit are dominant near the surface, whereas primary ores occur below $\sim$ 120 m. Oxidized ores are composed of acrusite, anglesine, siderite, smithsonite, calamine, hydrozinkite, antunesite, and malachite (Jin 2008). Massive and disseminated ores have similar mineral assemblages of sphalerite, galena, pyrite, calcite, and dolomite. Chalcopyrite, quartz, and fluorite are locally present. Sphalerite shows reflected light from light brown, dark brown to dark. Galena mainly occurs as massive aggregates associated with pyrite and locally is disseminated in sphalerite (Zhou et al. 2013, 2014). The paragenetic sequence in Tianqiao includes sedimentary diagenesis, hydrothermal mineralization, and oxidization stages (Zhou et al. 2013, 2014). The hydrothermal mineralization stage can be further divided into sulfide-carbonate and carbonate stages.

Wall rock alteration includes dolomite, calcite, Fe–Mn carbonate, and limonite. Fe–Mn carbonate and limonite are the main minerals indicating mineralization (Zhou et al. 2013). Fe–Mn carbonatization of the dolostone is considered to be key for mineralization by increasing the porosity of the wall rocks which facilitates further fluid infilling or replacement (Jin 2008). Ferritization results in Fe-capping of sulfide Pb–Zn ore bodies, which correlates positively with Pb–Zn mineralization.

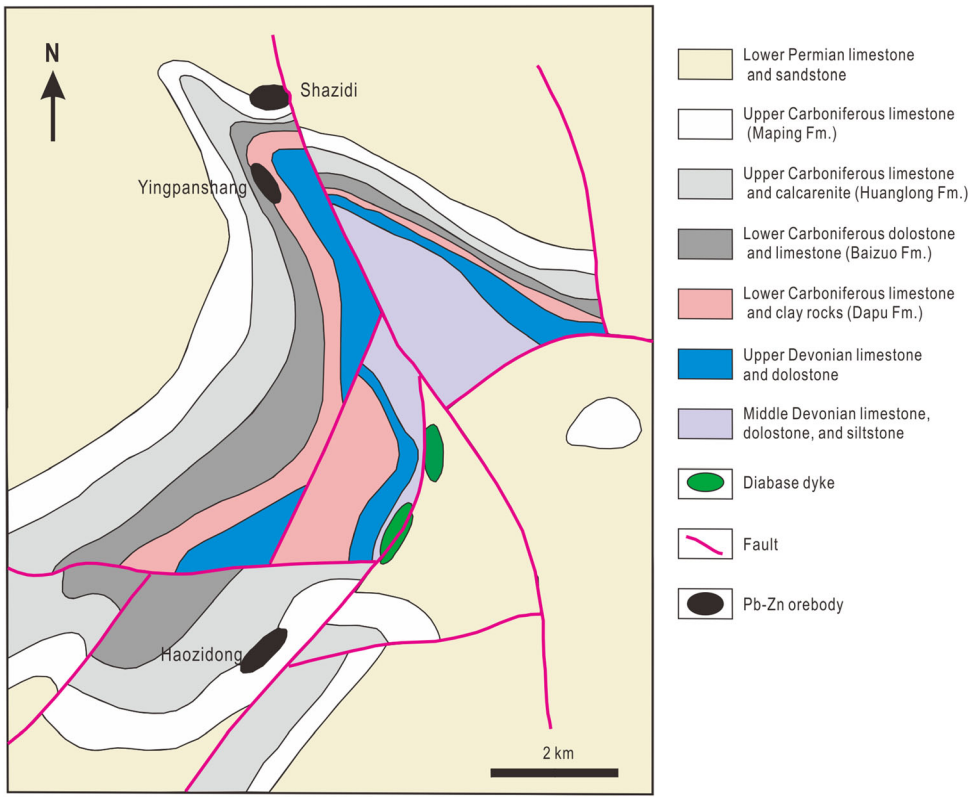

Fig. 2 A geological map of the Tianqiao Pb–Zn deposit showing the distribution of the major orebodies (modified from Jin, 2008)

3 Methods

3.1 Sampling

Six pyrite-bearing samples were collected from the Tianqiao deposit, while only one pyrite-bearing sample was from the Shanshulin deposit for comparison. These samples have various mineral assemblages and are related to different paragenetic stages of Zn–Pb mineralization. Major and trace element analyses of pyrite are carried out on the thin sections by EPMA and LA-ICP-MS, respectively. Pyrite samples for sulfur isotope analysis are separated by handpicking under an optical microscope, whereas some samples are prepared by micro-drilling.

3.2 EPMA analysis

Major and minor elements in pyrite were measured using a JEOL JXA-8230 EPMA at the Testing Center of Shandong Bureau of China Metallurgical Geology Bureau, Jinan, China. Elements were analyzed using the conditions same as those of Meng et al. (2018, 2019). The accelerating voltage is 15 kV, the beam current is 20 nA and the beam spot is 1 μm. JEOL ZAF software was used to correct matrix effects. Element content was calculated based on a series of SPI metal and mineral standards. The background time is 5–20 s and the peak time for element analysis is 10–40 s. The analysis yields an accuracy of 1–5 %. The detection limits are 36 ppm for S, 77 ppm for Ge and Au, ~ 90–100 ppm for As, Se, Ag, and Co, ~ 120–180 ppm for Fe, Ni, Cu, Zn, Cd, Sb, and Pb. Element mapping of a selected area was carried out using an accelerating voltage of 15 kV, a probe current of 100 nA, point size of 1 × 1 μm, and a dwell time of 3.3 ms for each point.

3.3 LA-ICP-MS analysis

Trace element contents of pyrite were determined with an Agilent 7700 × quadrupole ICP–MS coupled to a Photon Machines Excite 193 nm excimer laser ablation system at Nanjing FocuMs Technology, Nanjing, China. The analytical method is similar to that described by Meng et al. (2018), but the equipment types and analytical conditions for the laser ablation system and mass spectrometer are different. The analysis was performed using a laser ablation spot of 40 μm, a frequency of 8 Hz, and an energy intensity of ~ 5 mJ per pulse. The analysis time is 15 s for gas blank and 40 s for samples. Original data was dealt with using the software ICPMSDataCal (Liu et al. 2008), where elemental concentrations were calculated from signal intensities by external calibration against USGS GSE-1G (synthetic basaltic glass) and GSC 12,744 (pyrite) standards. The total contents of all the analyzed elements are

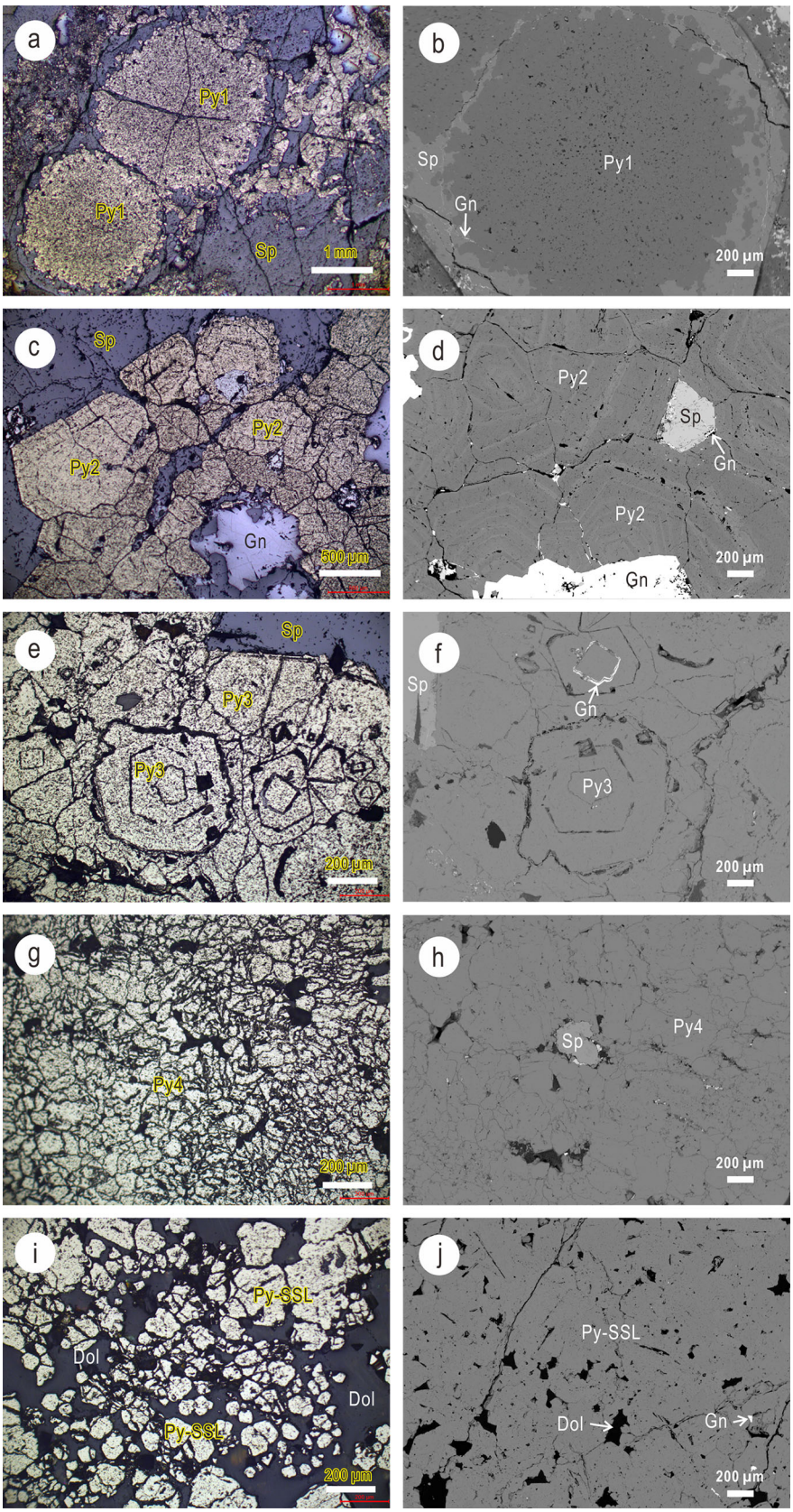

Fig. 3 Photomicrographs of reflected light (**a, c, e, g, i**) and back-scattered electron (**b, d, f, h**) showing the different types of pyrite in Tianqiao and Shanshuilin deposits. (**a, b**) The first type of pyrite (Py1) from the Tianqiao deposit shows framboid texture and is associated with sphalerite. (**c, d**) Second type of pyrite (Py2) from the Tianqiao deposit characterized by overgrowth textures. Py2 is in equilibrium with sphalerite and was replaced by galena. Oscillatory zoning is also identified in pyrite. (**e, f**) Third type of pyrite (Py3) from the Tianqiao deposit showing relic core-rim texture due to replacement. Galena grows along the fracture of pyrite due to previous replacement. (**g, h**) Fourth type of pyrite (Py4) from the Tianqiao deposit is dominated by subhedral to euhedral crystal with fracture texture. Sphalerite is locally present between pyrite grains. (**i, j**) Pyrite from the Shanshulin Pb–Zn (Py-SSL) deposit is subhedral disseminated in dolomite. Minor fine-grained galena occurs in the fracture of pyrite. Mineral abbreviations: Py, pyrite; Sp, sphalerite; Gn, galena; Dol, dolomite

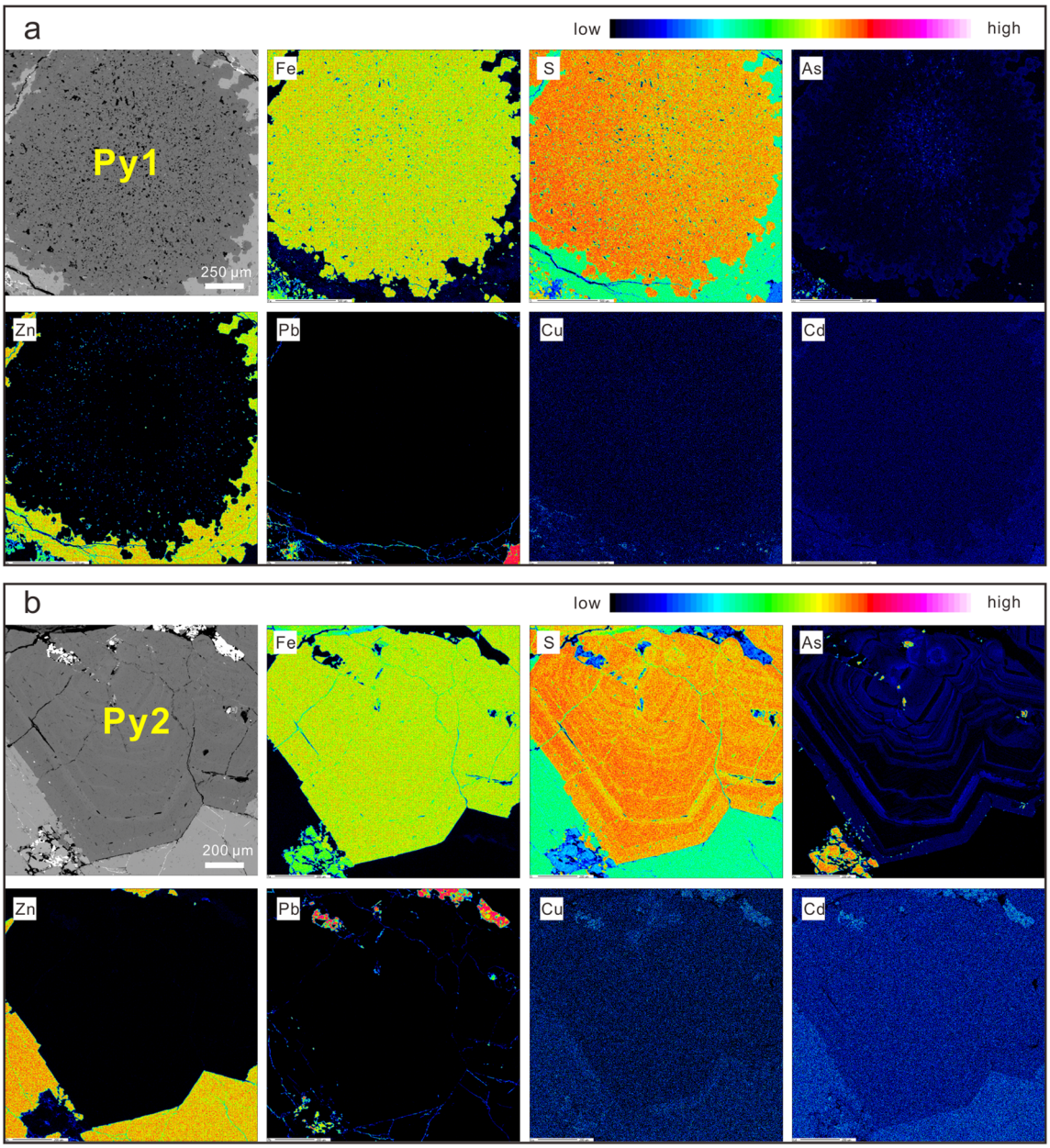

Fig. 4 Back-scattered electron images of pyrite and the wavelength dispersive X-ray elemental maps. **a** Py1 shows the relative enrichment of As in the core but depletion of Zn in the core (MYMTQ-9–1). **b** Py2 shows oscillatory zoning of S and As. Pb, Cu, and Cd are relatively homogenous (MYMTQ-9)

assumed to be 100 % to obtain the relative content of each element (Halicz and Günther 2004).

3.4 Sulfur isotope analysis

Sulfur isotopes were analyzed by a Thermo Scientific Flash 2000 high-temperature elemental analyzer coupled to a Thermo Scientific MAT 253 mass spectrometer at the SKLODG, IGCAS. The method used in this study was similar to that described by Huang et al. (2015). The sulfur isotopic compositions are reported as per mil (‰) relative to Vienna-Canyon Diablo Troilite (VCDT). The analytical precision is better than ± 0.2 ‰.

4 Results

4.1 Petrography

Reflected light microscope and BSE images reveal four types of pyrite (Py1 to Py4) in the Tianqiao deposit which have different textures and mineral assemblages. Py1 is a

Table 1 Average trace element contents (ppm) in different types of pyrite

Pyrite type	Ti	V	Cr	Mn	Co	Ni	Cu	Zn	Ga	Ge	As
Py1	13.8	0.13	13.9	2.7	0.04	1.0	155.9	8.8	0.20	4.1	14,686
Py2	16.6	0.37	6.0	4.0	0.05	0.6	102.6	5.2	0.03	3.1	9917
Py3	25.8	0.46	9.4	2.7	1.84	28.1	115.1	27.5	0.08	3.4	6144
Py4	13.1	0.40	10.1	4.3	0.14	0.7	10.3	8.0	0.10	3.7	85
Py-SSL	13.3	0.25	31.6	2.1	3.13	4.6	2.8	6.1	0.05	4.4	106

	Mo	Ag	Cd	In	Sn	Sb	Te	W	Au	Tl	Pb
Py1	0.02	16.0	13.0	0.10	0.36	14.8	0.23	0.03	0.07	0.20	97
Py2	0.04	47.1	0.12	0.01	0.23	17.0	0.49	0.06	0.04	0.06	91
Py3	1.42	10.7	0.20	0.02	0.28	62.5	0.70	0.05	0.18	0.22	278
Py4	0.04	7.8	0.19	0.02	0.43	4.6	0.50	0.95	0.05	0.16	379
Py-SSL	0.34	2.2	0.22	0.01	0.40	1.8	0.32	0.04	0.03	0.16	72

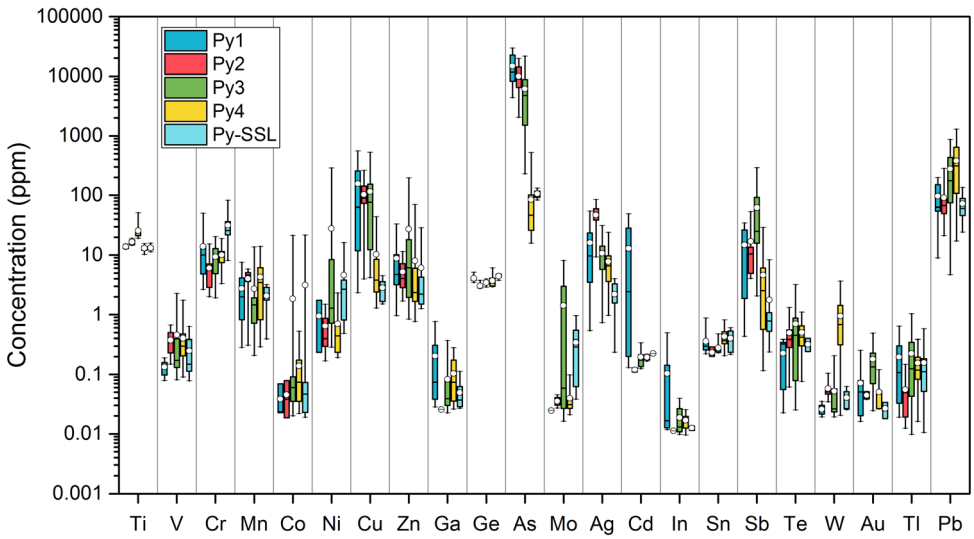

Fig. 5 Box and whisker plot showing the compositional differences between different types of pyrite. Boxes outline the 25th to 75th percentiles and whiskers extend to the minimum and maximum values. The short line in the box represents the median value, whereas the circle filled white represents the mean value

pyrite framboid, which was replaced by sphalerite (Fig. 3a, b). Py1 is coarse-grained with a diameter up to 1 mm. Py1 represents the pyrite formed at the sedimentary diagenesis stage. Py2 and Py3 represent pyrite with overgrowth and replacement relic textures, respectively (Fig. 3a, e), corresponding to the sulfide-carbonate stage. Py2 also shows oscillatory zoning under BSE imaging (Fig. 3d). Sphalerite and galena commonly grow in the space between pyrite grains or the fractures of pyrite (Fig. 3d, f). Py4 represents the euhedral pyrite of the sulfide-carbonate stage (Fig. 3g, h), which shows deformation and fragmentation texture. Pyrite from Shanshulin (Py-SSL) is subhedral and disseminated in dolomite (Fig. 3i, j), similar to Py4 but free of deformation.

4.2 EPMA results

Back-scattered electron microphotographs of pyrite and the wavelength dispersive X-ray elemental maps are shown in Fig. 4. The EPMA mapping of pyrite framboid (Py1) shows relatively enrichment of As in the core and Zn in the margin (Fig. 4a). Py2 has S and As contents distribution patterns consistent with zoning (Fig. 4a). Zinc, Pb, Cu, and Cd are not detectable in both Py1 and Py2, which indicates that no sphalerite, galena, and chalcopyrite inclusions in these two pyrite types (Fig. 4a). EPMA analyses of selected samples show that Py1, Py2, and Py3 have variable As contents from below detection limit to 4.94 wt%, whereas Py4 and Py-SSL have As contents below the detection limit (Appendix 1). Cobalt contents for all types of pyrite are below 0.2 wt%, whereas Ni, Cu, Zn, Au, Ag, Sb, Se, Ge, and Cd are mostly below the detection limit (Appendix 1). Lead contents for all pyrite types range from 0.08 to 0.53 wt%.

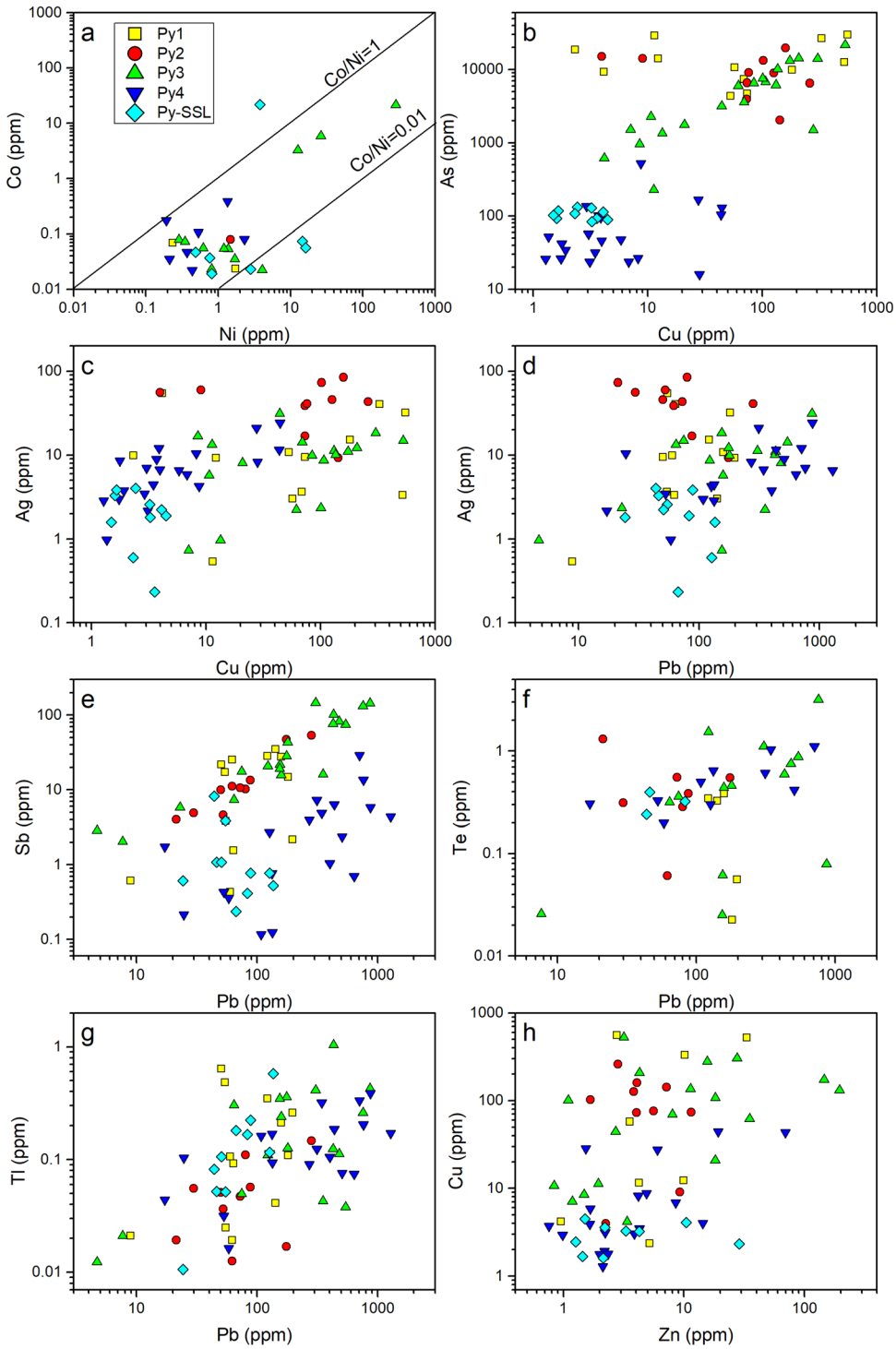

Fig. 6 Biplots showing the correlation between elements and compositional comparison for different types of pyrite

4.3 LA-ICP-MS results

Average trace element data for the pyrite samples are listed in Table 1. The trace element compositions of Py1 (n = 12), Py2 (n = 10), Py3 (n = 20), Py4 (n = 20), and one sample (n = 10) from Shanshulin Pb–Zn deposit were determined. Full spot analytical results of pyrite from the Tianqiao and Shanshulin deposits are listed in Appendix 2.

Pyrite from the Tianqiao and Shanshulin deposits contain a broad suite of measurable trace elements including Ti, V, Cr, Mn, Co, Ni, Cu, Zn, Ga, Ge, As, Mo, Ag, Cd, In, Sn, Sb, Te, W, Tl, and Pb. The trace element contents differ between the pyrite types (Fig. 5). Py1 is characterized by

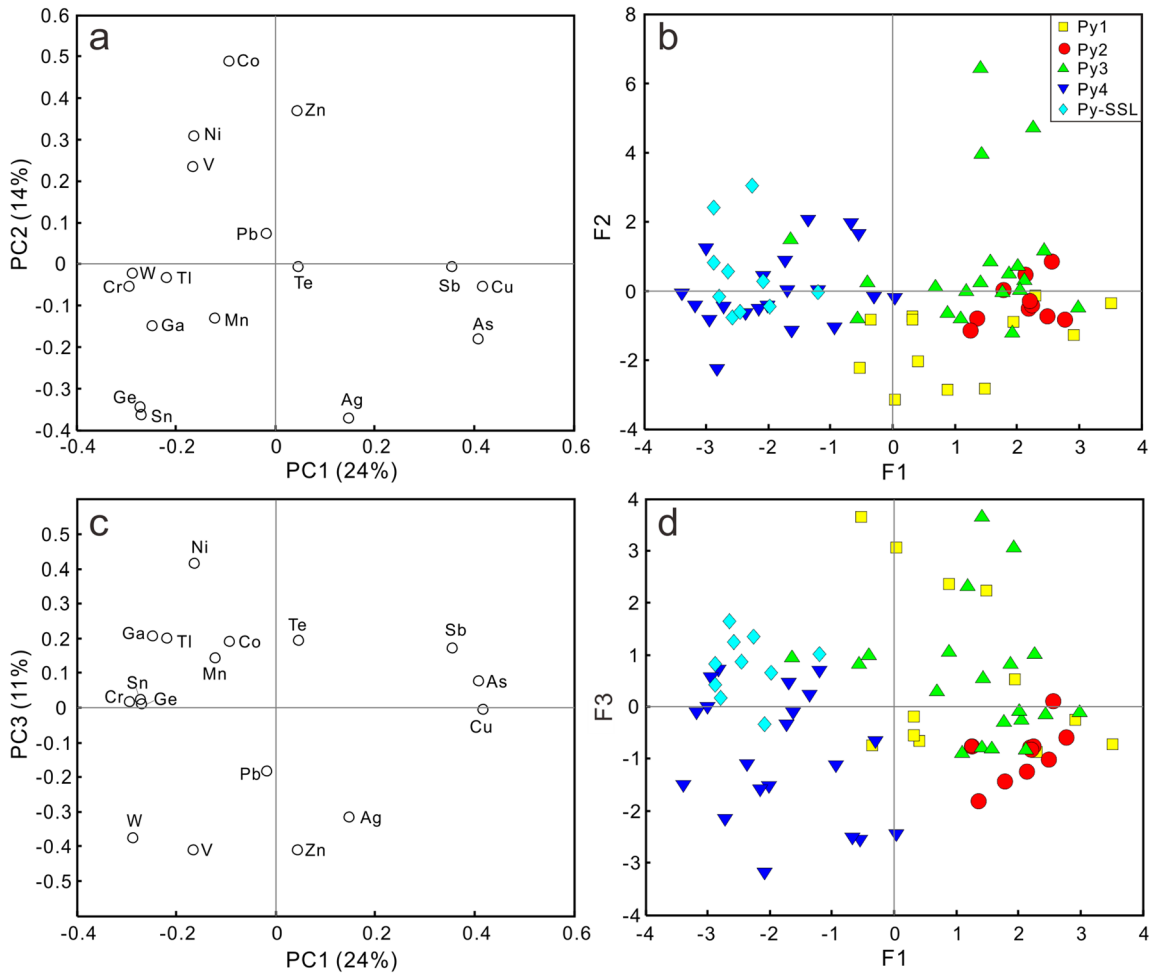

Fig. 7 **a** Loadings plot of the first and second principal components show element correlation. **b** Scores plot of the first and second principal components showing the distribution of different types of pyrite. **c** Loadings plot of the first and third principal components show element correlation. **d** Scores plot of the first and third principal components constrained by the correlation in **c**. Data in parentheses represent which degree a specific principal component accounts for the variation

relatively high average Cu, Ga, As, Cd, and In contents (Fig. 5). Py2 shows higher Ag content. Py3 has a higher average Co, Ni, Zn, Mo, and Sb contents than other pyrite types. Py4 has relatively high W content, whereas Py-SSL has higher Cr content (Fig. 5).

Nearly all pyrite types have Co/Ni ratios less than 1 (Fig. 6a). There is no obvious correlation between As and Cu for all types of pyrite (Fig. 6b). Copper and Ag are weakly correlated (Fig. 6c). Lead shows a weak correlation with Ag and Sb for Py3 and Py4 (Fig. 6d, e), whereas Pb is weakly correlated with Te for Py4 (Fig. 6f). No obvious correlation between Pb and Tl, and between Cu and Zn are identified for all types of pyrite (Fig. 6g, h).

To better identify the major features for different types of pyrite, principal component analysis (PCA) was conducted using LA-ICP-MS data. The data pretreatment method was the same as that described in Meng et al. (2019). Three components (PC1-PC3) were extracted using eigenvalues over 1, which accounts for 49 % of the variance in the dataset (Fig. 7). The biplots of loadings (e.g., PC1 vs. PC2) and scores (e.g., F1 vs. F2) for selected principal components are used to interpret the PCA results (Fig. 7). Different types of pyrite can be divided into two groups by first the principal component (Fig. 7a, b). Py1, Py2, and Py3 are characterized by relative enrichment of Sb, Cu, and As, in contrast to Py4 and Py-SSL which have relatively high Cr, W, Ge, Sn, Tl, Ni, and Ga contents (Fig. 7a, b). Samples from Py1 mainly plot in the positive F1, negative F2 region due to relatively high Cu, Ga, Ge, As, Ag, and Sn (Fig. 7a, b). Samples from Py2 have

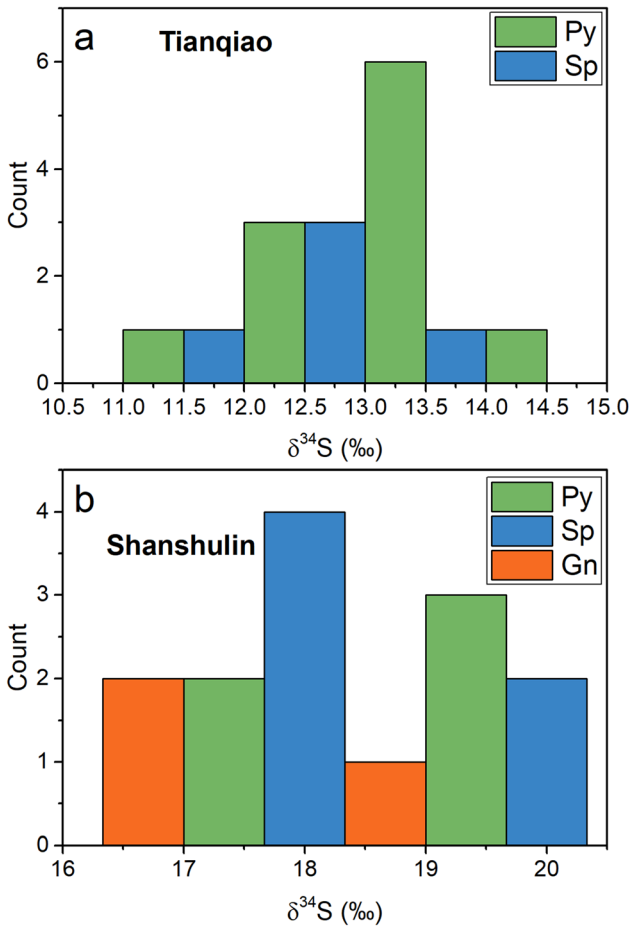

Fig. 8 Histogram showing sulfur isotope composition of sulfides from Tianqiao and Shanshulin deposits

relatively high Cu, As, Ag, whereas samples from Py3 show relative enrichment of Co, Cu, As, and Sb (Fig. 7a, b). Py4 can be distinguished from Py-SSL by the third principal component due to the relative W enrichment for the former and higher Cr, Ni, Ge, and Sn contents for the latter (Fig. 7c, d).

4.4 Sulfur isotope composition of sulfides

Sulfur isotope data for pyrite from the Tianqiao deposit are compiled in Appendix 3. In general, sulfides from the Tianqiao deposit have sulfur isotope composition clustering between 13.0 ‰ and 13.5 ‰ (Fig. 8a). Pyrite from the Tianqiao deposit yields $\delta^{34}S$ values of 11.8 ‰–14.4 ‰, similar to those (11.5 ‰–13.5 ‰) of sphalerite (Fig. 8a). In general, sulfides from the Shanshulin deposit have $\delta^{34}S$ values of 15.6 ‰–20.5 ‰, without compositional peak (Fig. 8b). Pyrite from the Shanshulin deposit has $\delta^{34}S$ values of 18.5 ‰–19.8 ‰, indistinguishable from those of sphalerite (18.6 ‰–20.5 ‰) (Fig. 8b). Galena from the Shanshulin deposit has a sulfur isotope composition ranging from 15.6 wt% to 17.1 wt% (Fig. 8b).

5 Discussion

5.1 The formation of pyrite with different textures

Four types of pyrite have different textures and mineral assemblages, indicating their formation at different stages of Pb–Zn mineralization due to different processes. Py1 has a characteristic framboid texture, typical of sedimentary diagenesis. Py2 has overgrowth texture and oscillatory zoning, indicating its formation by multiple hydrothermal fluids. Py3 has a zoned texture similar to those found in the Huize Pb–Zn deposit (Meng et al. 2019), which was possibly formed by fluid metasomatism. The existence of microinclusions of sphalerite and galena between the zoning of pyrite indicates that pyrite was replaced by Pb–Zn-rich fluids. Py4 was mainly formed from the hydrothermal process and was suffered from deformation to form fragmented texture. Pyrite from the Shanshulin deposit (Py-SSL) is closely associated with dolomite (Fig. 3i) and minor dolomite inclusions are also present in pyrite (Fig. 3j), indicating that pyrite was formed during dolomitization.

The overlapped trace element composition among Py1, Py2, and Py3 (Fig. 7b, d) indicates their compositional link. These three types of pyrite are enriched in As, Cu, and Sb relative to Py4 and Py-SSL (Figs. 6b, e, and 7b). It is inferred that the formation of Py2 and Py3 is possibly due to the replacement of Py1 or diagenetic fluids are involved during the precipitation of Py2 and Py3. Because there are no dissolution-reprecipitation textures or core-rim textures are found in Py2 and Py3 to show relics of Py1, the direct replacement of Py1 maybe not the major mechanism for the formation of Py2 and Py3. The involvement of the diagenetic component is evidenced by the sulfur isotope composition of pyrite. Ore pyrite including Py2 and Py3 has a sulfur isotope composition ranging from 11.8 to 14.4 ‰, consistent with derivation of sulfur from coeval seawater sulfate via thermochemical sulfide reduction or bacterial sulfate reduction (Zhou et al. 2018).

Contrary to Py1 to Py3, Py4 and Py-SSL are relatively enriched in Cr, W, Ge, Sn, and Ga, and are depleted in Sb, As, and Cu (Figs. 6b, e, 7). Py4 and Py-SSL are mainly associated with dolomite, and sphalerite and galena are locally present, possibly indicating the formation of Py4 and Py-SSL at the carbonate stage. The relative enrichment of dispersed elements such as Ga and Ge is likely due to less competition of these elements from sphalerite at the carbonate stage because these elements prefer partitioning into sphalerite (Meng et al. 2015). However, critical

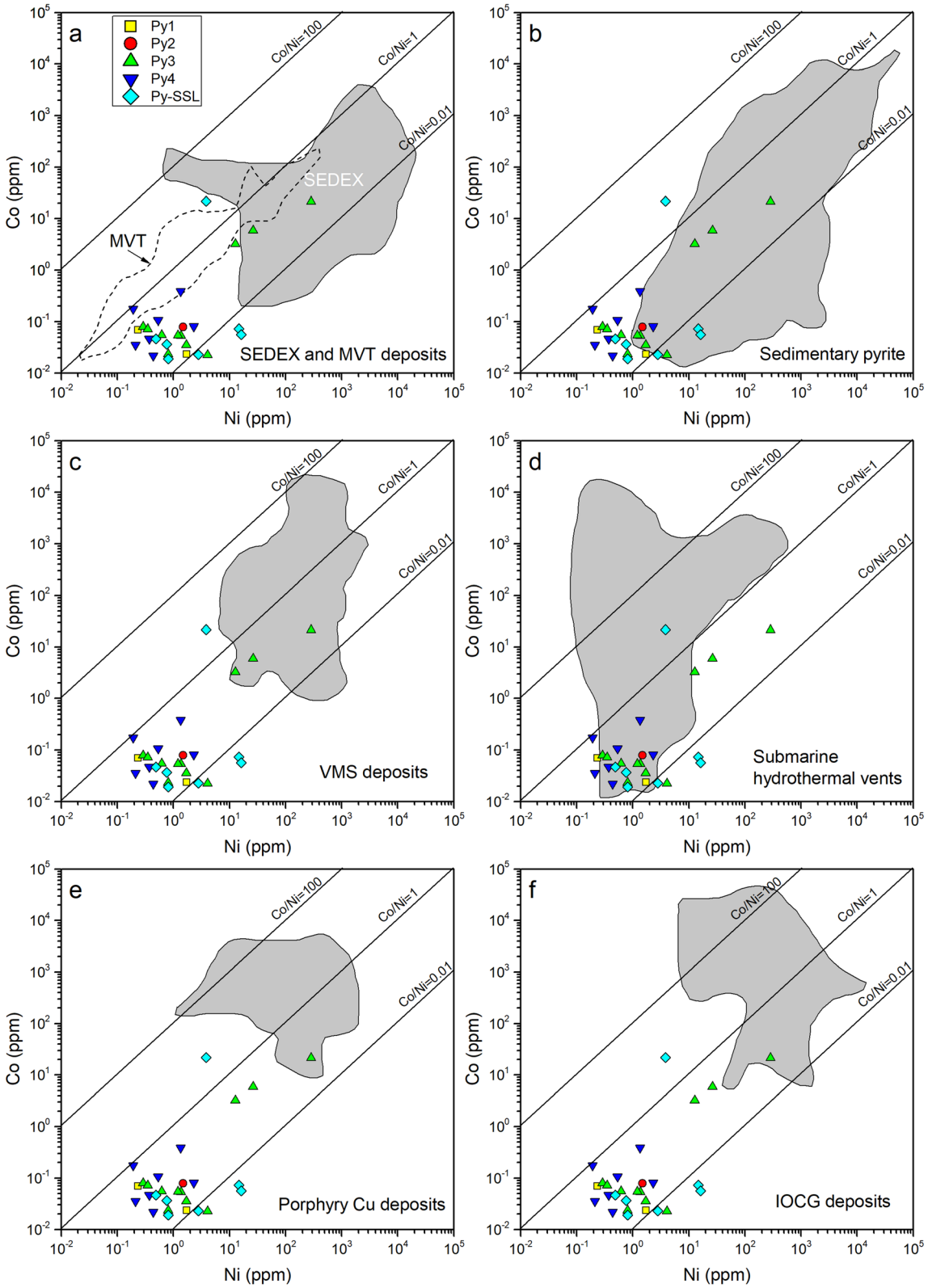

Fig. 9 Comparison of Co and Ni contents of pyrite from Tianqiao and Shanshulin deposits with that from other geological environments

elements such as Ga, Ge, and In are low in pyrite compared to those in sphalerite (Meng et al. 2015), indicating that pyrite is not the main host for these elements in the Tianqiao deposit.

In summary, textures and chemical composition of different types of pyrite record evolution from diagenetic fluids to Pb–Zn-rich hydrothermal fluids. Py1 was formed by sedimentary diagenesis, Py2 and Py3 were formed by multiple periods of hydrothermal fluids at the sulfide-carbonate stage, Py4 and Py-SSL were formed at the carbonate stage and suffered from deformation modification.

5.2 The origin of ore-forming fluids

Cobalt, Ni contents, and their ratios are important indicators for the origin of pyrite (Bajwah et al. 1987). Similar to Meng et al. (2019), pyrite Co and Ni values are compared with compiled data to determine the source of these metals (Fig. 9). Pyrite from Tianqiao and Shanshulin deposits have relatively low Co and Ni contents, different from pyrite from MVT, SEDEX, VMS, porphyry Cu, and IOCG deposits, but close to the lower part of sedimentary pyrite and pyrite from submarine hydrothermal vents (Fig. 9). Based on the deposit geology and tectonic setting, the Tianqiao and Shanshulin deposits are grouped as MVT deposits (Zhang et al. 2015; Li et al. 2016; Hu et al. 2017). The inconsistency between the geology and Co/Ni ratio discrimination indicates that only Co/Ni ratios cannot be used for discriminating different types of deposits, but can give some constraints on the nature of fluids. As shown in Fig. 9, low-temperature diagenetic-hydrothermal fluids such as those in the basin environment are responsible for the formation of pyrite. Sulfides from Tianqiao and Shanshulin are relatively enriched in heavy sulfur isotopes (Fig. 8), similar to most Pb–Zn deposits in the NW Guizhou district (Zhou et al. 2018). The sulfur of these deposits was mainly derived from the reduction of salt-gypsum rocks or coeval seawater sulfate. Considering Permian thrust tectonic movement is responsible for the formation of these Pb–Zn deposits, hydrothermal fluids for Py2, Py3, and Py-SSL are most likely formed via interaction with the host rocks containing salt-gypsum rocks. Therefore, combined trace elements and sulfur isotopes indicate that the Tianqiao and Shanshulin deposits were likely formed from low-temperature (e.g., < 250 °C) basin-like hydrothermal fluids via fluid-rock interaction.

6 Conclusions

Four types of pyrite (Py1 to Py4) are identified in the Tiaoqiao deposit, and one pyrite from the Shanshulin deposit (Py-SSL) is used for comparison. Textures, trace elements, and sulfur isotope compositions are used to constrain the origin of pyrite and ore-forming fluids. Py-SSL is comparable to Py4 in terms of textures, paragenetic stages, and chemical composition. Variation in trace element composition between different pyrite types results from fluid evolution from diagenetic to hydrothermal fluids where co-precipitating minerals also play some role. During fluid evolves, Sb As, and Cu in the fluids decreased whereas Ga and Ge increased. By comparison with pyrite from different geological environments, we argue that ore-related pyrite from Tiaoqiao (Py2 and Py3) and Shanshulin (Py-SSL) deposits are derived from relatively low-temperature (e.g., $< \sim 250$ °C) hydrothermal fluids like basin brines or seawater via fluid-rock interaction. High-temperature magma-related high-temperature hydrothermal fluids are not involved in the formation of pyrite.

Appendix 1

See Table 2.

Table 2 EPMA analytical results (wt%) of pyrite from the Tianqiao and Shanshulin Zn–Pb–Ag deposits

Sample no.	Pyrite type	Fe	S	As	Co	Ni	Cu	Zn	Au	Ag	Sb	Pb	Se	Ge	Cd	Total
Tianqiao deposit																
MYMTQ-9–1	Py1	45.2	49.2	4.94	0.065	bdl	bdl	bdl	bdl	bdl	bdl	0.172	bdl	bdl	bdl	99.6
MYMTQ-9–1	Py1	45.5	52.8	bdl	0.062	bdl	bdl	0.055	0.013	0.011	bdl	0.139	bdl	bdl	0.076	98.7
MYMTQ-9–1	Py2	45.1	51.5	1.301	0.048	bdl	bdl	bdl	bdl	bdl	bdl	0.088	bdl	bdl	bdl	98.1
MYMTQ-9	Py2	44.5	49.8	4.127	0.031	0.022	0.138	bdl	bdl	bdl	0.028	0.126	bdl	bdl	0.051	98.8
MYMTQ-9	Py2	44.3	50.7	3.147	0.044	bdl	0.019	bdl	0.011	bdl	bdl	0.141	bdl	bdl	bdl	98.4
MYMTQ-12–1	Py3	45.4	52.6	bdl	0.042	bdl	0.057	bdl	bdl	bdl	bdl	0.109	bdl	0.01	bdl	98.2
MYMTQ-12–1	Py3	44.8	49.6	4.764	0.027	bdl	0.045	bdl	bdl	0.033	bdl	0.172	bdl	bdl	bdl	99.5
MYMTQ-12–1	Py3	45.8	53.2	bdl	0.024	bdl	0.039	bdl	0.011	bdl	bdl	0.099	bdl	bdl	0.078	99.3
MYMTQ-12–1	Py3	45.6	52.9	bdl	0.032	bdl	bdl	bdl	bdl	bdl	0.019	0.178	bdl	0.04	0.07	98.9
MYMTQ-12	Py3	44.9	51.7	1.078	0.055	bdl	bdl	0.028	bdl	bdl	bdl	0.204	bdl	bdl	0.017	98.0
MYMTQ-12	Py3	45.0	52.0	0.36	0.023	bdl	bdl	0.06	0.02	0.01	bdl	0.526	bdl	bdl	bdl	98.1
MYMTQ-12	Py3	45.5	52.2	0.411	0.047	bdl	bdl	bdl	0.019	bdl	bdl	0.125	0.022	bdl	bdl	98.3
MYMTQ-12	Py3	45.8	52.8	bdl	bdl	bdl	bdl	bdl	0.009	bdl	bdl	0.134	bdl	bdl	bdl	98.8
MYMTQ-12	Py3	44.7	50.2	2.504	0.064	bdl	bdl	0.069	bdl	bdl	bdl	0.164	bdl	bdl	0.055	97.8
FSLTQ-15	Py4	45.8	52.8	bdl	0.053	bdl	bdl	bdl	bdl	0.02	bdl	0.136	bdl	bdl	bdl	98.8
FSLTQ-15	Py4	45.7	53.0	bdl	0.054	bdl	0.034	0.035	bdl	0.01	bdl	0.138	bdl	0.051	0.018	99.0
FSLTQ-15	Py4	43.5	51.0	bdl	0.145	bdl	bdl	bdl	0.013	0.028	0.034	0.107	0.012	bdl	bdl	94.8
MYMTQ-8	Py4	46.4	52.9	bdl	0.028	bdl	0.024	0.055	bdl	bdl	bdl	0.081	bdl	bdl	0.02	99.6
Shanshulin deposit																
SSL-1	Py-SSL	47.2	53.6	bdl	0.057	0.014	0.018	bdl	bdl	bdl	0.043	0.131	bdl	bdl	bdl	101.0
SSL-1	Py-SSL	47.0	52.8	bdl	0.031	bdl	bdl	0.061	bdl	bdl	bdl	0.113	bdl	bdl	0.033	100.1
SSL-1	Py-SSL	46.8	53.5	bdl	0.074	bdl	0.034	bdl	0.01	bdl	bdl	0.122	bdl	bdl	bdl	100.6

"bdl" means one element has content below detection limit

Appendix 2

See Table 3.

Table 3 The trace element compositions of pyrite from the Tianqiao and Shanshulin Zn–Pb–Ag deposits

	Sample no	Ti	V	Cr	Mn	Co	Ni	Cu	Zn	Ga	Ge	As	Mo	Ag	Cd	In	Sn	Sb	Te	W	Tl	Pb
Pyrite type	Detection limit	0.89	0.07	1.17	0.19	0.02	0.07	0.07	0.69	0.02	0.38	0.93	0.015	0.018	0.109	0.009	0.19	0.043		0.017		0.024
Tianqiao deposit																						
Py1	TQ-9–1-01	12.68			4.12		0.87	73.71		0.76	4.61	4705		9.41	49.33	0.49	0.87	21.70		0.04	0.64	50.43
Py1	TQ-9–1-02	13.51	0.16		1.17	0.07	0.24	329.51	10.20		3.69	26,638		40.47		0.02	0.30	1.56		0.02	0.09	64.01
Py1	TQ-9–1-03	12.86		12.32				57.27	3.57	0.05	4.17	10,658		2.99	0.13	0.01		34.81	0.33	0.02	0.04	142.26
Py1	TQ-9–1-04	13.88						521.54	33.26		4.25	12,578		3.33	0.20	0.02		25.12			0.02	62.57
Py1	TQ-9–1-05	13.07		50.68	3.89	0.02	1.74	69.19		0.42	5.14	7290		3.64	28.48	0.28	0.37	17.12			0.48	54.44
Py1	TQ-9–1-06	13.05		7.75	1.67			53.04		0.19	4.00	4375		10.82	9.85	0.14	0.30	27.51	0.38		0.21	159.46
Py1	TQ-9–1-07	13.91		15.74	0.82			181.83		0.10	4.16	9866	0.02	15.20	2.43	0.11	0.25	28.36	0.35		0.35	122.15
Py1	TQ-9–1-08	15.42	0.14	4.04	2.33			4.16	0.96	0.03	3.45	9175		54.93			0.30	3.82			0.02	55.00
Py1	TQ-9–1-09	14.33	0.13		0.28			11.50	4.25		3.80	28,948		0.53	0.44	0.01	0.26	0.61			0.02	8.94
Py1	TQ-9–1-10	14.33	0.08	5.64	0.58			554.88	2.78	0.03	3.92	29,568		31.90		0.01		14.70	0.02		0.11	181.40
Py1	TQ-9–1-11	14.85	0.19	2.63	7.55	0.02		2.34	5.20		3.77	18,450		9.92		0.01	0.22	0.43			0.11	60.17
Py1	TQ-9–1-12	13.61	0.10	12.77	4.88			12.31	10.01	0.05	4.03	13,983		9.18		0.01		2.18	0.06	0.02	0.26	197.60
Py2	MYMTQ-9–01	19.22	0.23	5.10	5.67	0.02		159.35	4.09		3.76	19,554		85.04				10.29	0.28		0.11	79.93
Py2	MYMTQ-9–02	18.13	0.45	1.98	4.71		0.17	102.18	1.68		3.08	13,330	0.05	73.48				4.04	1.32	0.05	0.02	21.29
Py2	MYMTQ-9–03	17.89	0.19	7.12	4.58	0.04		126.02	3.84		2.93	8989	0.04	46.08				9.96			0.05	50.02
Py2	MYMTQ-9–04	17.90	0.48	9.20	3.60	0.08	1.48	260.64	2.83		2.99	6528		43.54	0.11			10.61	0.56		0.05	72.76
Py2	MYMTQ-9–05	16.03	0.23	2.87	5.84			9.04	9.24		2.93	14,167	0.03	59.99				4.64		0.05	0.04	52.44
Py2	MYMTQ-9–06	15.46	0.52	6.90	4.78		0.87	73.57	11.51	0.03	2.95	6543		38.97		0.01	0.21	11.16	0.06	0.10	0.01	62.01
Py2	MYMTQ-9–07	16.09	0.67	15.33	0.31		0.40	142.49	7.16		2.86	2042		9.31			0.29	47.14	0.55	0.03	0.02	175.73
Py2	MYMTQ-9–08	15.28	0.33	2.52	2.26			73.05	4.04		3.09	3935		16.92	0.13			13.54	0.38		0.06	87.67
Py2	MYMTQ-9–09	15.14	0.50	6.15	5.08		0.30	76.07	5.62		3.21	9002		41.06			0.20	53.51			0.15	281.92
Py2	MYMTQ-9–10	14.61	0.15	3.30	3.62			3.97	2.25		2.74	15,082	0.03	56.34				4.92	0.31	0.05	0.06	29.78
Py3	TQ12-1–01	29.03	0.25	13.62	1.49	0.11		69.47	8.04		3.78	3591		14.21	0.21	0.03	0.47	74.39	0.87	0.07	0.04	543.24
Py3	TQ12-1–02	27.49	0.16	7.60	0.27	0.09		44.23	2.71		3.97	3182		31.29			0.24	144.63	0.08	0.02	0.43	866.65
Py3	TQ12-1–03	25.87	0.40	8.83	13.68	0.04	1.70	11.33	1.95	0.02	3.59	229	0.02	13.30			0.24	7.35	0.32		0.30	64.49
Py3	TQ12-1–04	26.19		2.96	5.49	0.02	4.08	84.30		0.03	3.28	6559	0.06	9.84	0.31		0.23	43.18	0.46	0.02	0.13	179.58
Py3	TQ12-1–05	26.86	0.12	11.00	1.92			20.87	18.18	0.03	3.93	1769	0.10	8.07	0.21			82.61	0.75	0.02	0.11	481.11
Py3	TQ12-1–06	24.70	0.13	14.68	1.45	0.08	0.29	106.74	18.25	0.08	3.74	6790		8.65		0.02	0.26	20.57	1.53		0.11	122.88
Py3	TQ12-1–07	24.35	0.12	4.07	0.61	0.04		7.09	1.19	0.03	3.00	1523		0.73				21.67	0.06			154.96
Py3	TQ12-1–08	22.31		1.92	9.86	0.05	1.38	10.70	0.84		3.48	2274	0.05	5.76		0.04		15.69	0.44		0.24	158.58
Py3	TQ12-1–09	21.17	0.08	8.86	1.33	0.07	0.35	8.50	1.48	0.03	3.30	957		16.88	0.16	0.01		291.24		0.06	0.01	
Py3	TQ12-1–10	23.11	0.16	8.28	0.21		0.94	13.42			3.15	1345.88	0.03	0.97				2.87		0.03	0.01	4.71
Py3	MYMTQ-12–01	38.30	1.37	12.14	1.47	0.06		208.05	4.29	0.11	3.40	14,141		12.18			0.23	28.29		0.03	0.36	176.10
Py3	MYMTQ-12–02	21.73	0.17	4.77	0.49	0.08		61.63	35.16	0.03	3.08	5948	0.05	2.22	0.13		0.28	16.16			0.04	353.65
Py3	MYMTQ-12–03	21.14	0.22	4.43				100.98	1.10	0.05	3.88	7488		2.32	0.14			5.81		0.06		22.96
Py3	MYMTQ-12–04	19.64	0.17	5.99	1.43	0.02		528.61	3.18	0.05	2.89	21,511	0.03	14.84				17.56	0.36	0.02	0.05	74.67
Py3	MYMTQ-12–05	23.26	1.05	4.99	1.58	21.38	287.02	278.29	15.64	0.03	3.28	1492	3.00				0.29	132.96	3.19		0.26	758.34
Py3	MYMTQ-12–06	24.35	0.29	15.74	0.71	0.06	0.62	304.16	27.62	0.05	3.28	14,035	0.07	18.45	0.12		0.28	19.13	0.03		0.35	154.36

Table 3 continued

Pyrite type	Sample no Detection limit	Ti 0.89	V 0.07	Cr 1.17	Mn 0.19	Co 0.02	Ni 0.07	Cu 0.07	Zn 0.69	Ga 0.02	Ge 0.38	As 0.93	Mo 0.015	Ag 0.018	Cd 0.109	In 0.009	Sn 0.19	Sb 0.043	Te	W 0.017	Tl	Pb 0.024
Py3	MYMTQ-12–07	51.33	0.99	15.15	1.76	5.91	26.42	131.19	195.62	0.25	3.50	6102	8.11	11.27	0.34			145.54	1.10	0.09	0.41	306.56
Py3	MYMTQ-12–08		2.25	20.30	3.68	3.24	12.66	173.67	145.70	0.37	3.32	13,178	4.08	11.08	0.18	0.01	0.27	101.31	0.59	0.21	1.04	431.69
Py3	MYMTQ-12–09	19.22	0.16	11.15	1.18	0.05	1.21	135.50	11.33		3.28	10,144		10.10	0.16	0.01		76.23		0.04	0.12	427.13
Py3	MYMTQ-12–10	19.22	0.13	11.64		0.02	0.81	4.17	3.38		3.44	614						2.05	0.03	0.02	0.02	7.69
Py4	MYMTQ-8–01	14.74	0.10	4.09	10.26	0.03		8.24	4.19	0.08	3.02	26.45	0.03	10.41				0.22		0.77	0.10	24.71
Py4	MYMTQ-8–02	13.54	0.49	18.86	1.44	0.53		44.26	19.30		5.36	127.89		24.19	0.19			5.79		3.65	0.39	872.17
Py4	MYMTQ-8–03	14.28	0.36	7.37				27.64	6.04		3.01	165.86	0.05	21.07	0.22		0.37	7.27	0.61	2.20	0.12	313.59
Py4	MYMTQ-8–04	13.87		4.12		0.02	0.44	3.11	2.22		3.43	23.53		2.16				1.74	0.30	0.02	0.04	17.17
Py4	MYMTQ-8–05	14.58	0.58	8.62	1.20		0.67	28.29	1.54	0.06	3.92	15.88	0.03	8.30			0.52	3.93		1.55	0.09	272.00
Py4	MYMTQ-8–06	13.25	0.69	6.28	0.56		0.24	5.83	1.67	0.07	3.20	47.92	0.03	6.54			0.81	4.37		0.43	0.17	1286.06
Py4	MYMTQ-8–07	14.24	1.74	11.51	0.82	0.05	0.37	43.59	69.68	0.17	2.99	103.01	0.03	11.59				6.33		1.00	0.19	437.11
Py4	MYMTQ-8–08	12.20	0.45	8.20				1.92	2.19	0.03	2.94	34.10		3.76			0.45	1.04		0.35	0.11	402.03
Py4	MYMTQ-8–09	13.72	0.19	10.44				8.72	4.90	0.03	3.35	520.42		4.25		0.01		2.71	0.30	0.02	0.11	126.77
Py4	MYMTQ-8–10	15.61	0.47	8.21				6.82	8.57	0.04	3.07	23.75		5.87				0.70		2.72	0.07	639.63
Py4	FSLTQ-15–01	13.89	0.10	8.44	0.29			2.91	0.98	0.03	3.79	134.69		3.44			0.21	0.43	0.33		0.03	52.85
Py4	FSLTQ-15–02	13.67	0.22	11.36	7.30	0.17	0.19	3.04	3.88	0.21	3.62	57.25		6.98		0.02		13.49		0.68	0.20	761.88
Py4	FSLTQ-15–03	12.91	0.09	3.32				3.71	0.76		3.12	100.45		8.97	0.20	0.03	0.37	2.38	0.42	0.34	0.08	508.40
Py4	FSLTQ-15–04	11.68	0.27	10.89	5.14	0.07		3.47	4.28	0.10	2.94	31.75	0.10	4.45			0.33	0.12		0.76	0.09	133.83
Py4	FSLTQ-15–05	10.29	0.32	18.74	5.54	0.11	0.53	3.90	1.65	0.28	4.56	94.66		12.01		0.02	0.62	29.12	1.11	1.20	0.33	709.69
Py4	FSLTQ-15–06	12.65		15.23	0.55			1.36			3.74	51.84		0.98	0.17		0.44	0.36	0.20	0.04	0.02	58.38
Py4	FSLTQ-15–07	12.01	0.27	7.63	13.99	0.05		1.28	2.12	0.20	4.22	25.81	0.02	2.83		0.01	0.33	0.76	0.64	0.39	0.17	133.15
Py4	FSLTQ-15–08	11.65	0.40	11.37	4.30	0.08	2.31	1.75	2.00		2.92	26.13		2.96			0.24	0.12	0.50	0.10	0.16	107.99
Py4	FSLTQ-15–09	12.26	0.20	15.84	2.63	0.39	1.35	3.96	14.40	0.04	4.60	46.07		6.66				4.88	1.03	0.31	0.32	344.34
Py4	FSLTQ-15–10	10.77	0.27	10.77	6.17	0.04	0.21	1.78	2.35	0.11	6.09	41.69	0.02	8.54		0.02		6.80	0.08	1.42	0.30	
Shanshulin deposit																						
Py-SSL	SLL-1–01	15.78	0.22	8.15	1.76	0.04	0.76	3.58	2.20	0.04	3.95	92.81	0.39	0.23		0.01		0.24			0.18	66.93
Py-SSL	SLL-1–02	14.02	0.08	43.93	1.04	0.05	0.48	3.26	3.29		4.39	83.24	0.96	1.81				0.61		0.05	0.01	24.28
Py-SSL	SLL-1–03	13.42	0.11	25.88	1.98		1.21	4.47	1.51	0.06	3.76	89.36	0.69	1.88			0.53	0.42	0.32		0.17	83.00
Py-SSL	SLL-1–04	14.26	0.12	36.60	3.18		2.55	1.60	2.13	0.03	4.67	91.94	0.55	3.28			0.43	1.08	0.40	0.03	0.05	46.24
Py-SSL	SLL-1–05	12.36	0.11	22.01	0.39		2.95	2.43	1.27	0.03	4.30	131.73	0.06	4.00		0.01		8.29	0.24	0.03	0.08	43.86
Py-SSL	SLL-1–06	11.77	0.42	25.70	2.91	0.02	0.81	1.66	1.44	0.03	4.42	117.02	0.04	3.84			0.23	0.78			0.22	88.60
Py-SSL	SLL-1–07	11.42		26.91		0.02	2.80	3.23	4.25	0.03	4.56	128.84	0.29	2.56			0.60	3.84		0.06	0.05	54.53
Py-SSL	SLL-1–08	13.46	0.63	82.38	2.57	0.07	14.65	2.31	28.68	0.07	4.51	107.58	0.05	0.60	0.22			0.77			0.12	127.09
Py-SSL	SLL-1–09	13.27	0.38		2.87	0.06	16.15	1.50			4.71	102.44		1.58				0.53		0.03	0.58	135.68
Py-SSL	SLL-1–10	12.97	0.15	13.10	1.91	21.67	3.80	4.08	10.45	0.11	4.82	113.40	0.07	2.22			0.22	1.08		0.05	0.11	50.66

Appendix 3

See Table 4.

Table 4 Sulfur isotope composition of sulfides from the Tianqiao and Shanshulin deposits

Smaple nos	$\delta^{34}S_{V\text{-}CDT}$ (‰)	Stage	References
Tianqiao deposit			
HTQ-T7S	13.4	Ore pyrite	Gu (2004)
TQ-18–1	13.7	Ore pyrite	Zhou et al. (2010)
TQ-19	14.4	Ore pyrite	Zhou et al. (2010)
TQ-23	12.8	Ore pyrite	Zhou et al. (2010)
TQ-24–1	12.9	Ore pyrite	Zhou et al. (2010)
TQ-60–1	13.2	Ore pyrite	Zhou et al. (2013)
TQ-12–1	13	Ore pyrite	This study
TQ-8	13.3	Ore pyrite	This study
MYMTQ-12	13.4	Py3	This study
MYMTQ-9	11.8	Py2	This study
TQ-12–1	13.0	Py3	Meng (2014)
TQ-8	13.5	Ore sphalerite	Meng (2014)
TQ-9	11.5	Ore sphalerite	Meng (2014)
TQ-10	12.3	Ore sphalerite	Meng (2014)
TQ-11	12.3	Ore sphalerite	Meng (2014)
TQ-12	12.2	Ore sphalerite	Meng (2014)
Shanshulin deposit			
SSL-1	19.0	Ore sphalerite	Meng (2014)
SSL-2	19.3	Ore sphalerite	Meng (2014)
SSL-3	18.7	Ore sphalerite	Meng (2014)
SSL-4	18.6	Ore sphalerite	Meng (2014)
SSL-6	20.5	Ore sphalerite	Meng (2014)
SSL-8	18.8	Ore sphalerite	Meng (2014)
SSL-4	18.5	Ore pyrite	Meng (2014)
SSL-6	19.6	Ore pyrite	Meng (2014)
SSL-1	15.6	Ore galena	Meng (2014)
SSL-3	15.7	Ore galena	Meng (2014)
SSL-6	17.1	Ore galena	Meng (2014)
SSL-4	18.5	Ore pyrite	This study
SSL-6	19.6	Ore pyrite	This study
SSL-1	19.8	Ore pyrite	This study

Acknowledgements This research was financially supported by the Department of Science and Technology of Guizhou Province (Guizhou Science Foundation No. 20171197), CAS Hundred Talents Program (No. Y9CJ034000) to XWH, Science and Technique Foundation of Water Resources Department of Jiangxi Province (No. 202123YBKT10), National Natural Science Foundation of China (Nos. 42073043; 41673050). Thanks are given to Dr. Jing Gu for sulfur isotope analyses. We thank Prof. Jian-Feng Gao and Prof. Liang Li for their help during LA-ICP-MS trace element analyses. Wanting Ge and Yan Liu are thanked for micro-drill sampling for sulfur isotope analyses. Two anonymous reviewers are thanked for their critical comments which have improved the manuscript.

Funding Guizhou Science Foundation, 20171197, Yumiao Meng, CAS Hundred Talents Program, Y9CJ034000, Xiao-Wen Huang, National Natural Science Foundation of China, 42073043, Yumiao Meng, 41673050, Xiao-Wen Huang, Science and Technique Foundation of Water Resources Department of Jiangxi Province, 202123YBKT10, Chun-Xia Xu

Declarations

Conflict of interest On behalf of all authors, the corresponding author states that there is no conflict of interest.

References

Abraitis PK, Pattrick RAD, Vaughan DJ (2004) Variations in the compositional, textural and electrical properties of natural pyrite: a review. Int J Mineral Process 74:41–59

Bajwah Z, Seccombe P, Offler R (1987) Trace element distribution Co: Ni ratios and genesis of the Big Cadia iron-copper deposit, New South Wales, Australia. Miner Deposita 22:292–300

Baker T, Mustard R, Brown V, Pearson N, Stanley C, Radford N, Butler I (2006) Textural and chemical zonation of pyrite at Pajingo: a potential vector to epithermal gold veins. Geochem Explor Environ Anal 6:283–293

Bao Z, Li Q, Wang CY (2017) Metal source of giant Huize Zn–Pb deposit in SW China: New constraints from in situ Pb isotopic compositions of galena. Ore Geol Rev 91:824–836

Chung SL, BM Jahn (1995) Plume-lithosphere interaction in generation of the Emeishan flood basalts at the Permian-Triassic boundary. Geology 23:889–892

Cook NJ, Ciobanu CL, Pring A, Skinner W, Shimizu M, Danyushevsky L, Saini-Eidukat B, Melcher F (2009) Trace and minor elements in sphalerite: A LA-ICPMS study. Geochim Cosmochim Acta 73:4761–4791

Cook N, Ciobanu CL, George L, Zhu Z-Y, Wade B, Ehrig K (2016) Trace element analysis of minerals in magmatic-hydrothermal ores by laser ablation inductively-coupled plasma mass spectrometry: approaches and opportunities. Minerals 6:111

Deditius AP, Reich M, Kesler SE, Utsunomiya S, Chryssoulis SL, Walshe J, Ewing RC (2014) The coupled geochemistry of Au and As in pyrite from hydrothermal ore deposits. Geochim Cosmochim Acta 140:644–670

Franchini M, McFarlane C, Maydagán L, Reich M, Lentz DR, Meinert L, Bouhier V (2015) Trace metals in pyrite and marcasite from the Agua Rica porphyry-high sulfidation epithermal deposit, Catamarca, Argentina: Textural features and metal zoning at the porphyry to epithermal transition. Ore Geol Rev 66:366–387

Gao S, Yang J, Zhou L, Li M, Hu Z, Guo J, Yuan H, Gong H, Xiao G, Wei J (2011) Age and growth of the Archean Kongling terrain, South China, with emphasis on 3.3 Ga granitoid gneisses. Am J Sci 311:153–182

Gregory DD, Large RR, Bath AB, Steadman JA, Wu S, Danyushevsky L, Bull SW, Holden P, Ireland TR (2016) Trace element content of pyrite from the kapai slate, St. Ives Gold District. Western Australia Econ Geol 111:1297–1320

Gu SY (2004) Characteristicsof rare-earth elements composition within lead-zinc deposits in Northwestern Guizhou: in addition to a discussionof relationship between lead-zinc depositsand Emeishan basalts in Northwestern Guizhou. Guizhou Geol 23:274–277 ((**in Chinese with English Abstract**))

Halicz L, Günther D (2004) Quantitative analysis of silicates using LA-ICP-MS with liquid calibration. J Anal at Spectrom 19:1539–1545

Han RS, Liu CQ, Huang ZL, Chen J, Ma DY, Lei L, Ma GS (2007) Geological features and origin of the Huize carbonate-hosted Zn–Pb-(Ag) District, Yunnan, South China. Ore Geol Rev 31:360–383

Hu R, Fu S, Huang Y, Zhou M-F, Fu S, Zhao C, Wang Y, Bi X, Xiao J (2017) The giant South China Mesozoic low-temperature metallogenic domain: Reviews and a new geodynamic model. J Asian Earth Sci 137:9–34

Huang X-W, Zhou M-F, Qiu Y-Z, Qi L (2015) In-situ LA-ICP-MS trace elemental analyses of magnetite: The Bayan Obo Fe-REE-Nb deposit, North China. Ore Geol Rev 65:884–899

Huston DL, Sie SH, Suter GF, Cooke DR, Both RA (1995) Trace elements in sulfide minerals from eastern Australian volcanic-hosted massive sulfide deposits; Part I, Proton microprobe analyses of pyrite, chalcopyrite, and sphalerite, and Part II, Selenium levels in pyrite; comparison with delta 34 S values and implications for the source of sulfur in volcanogenic hydrothermal systems. Econ Geol 90:1167–1196

Jin Z (2008) The Ore-control Factors, Ore-forming Regularity and Forecasting of Pb–Zn Deposit, in Northwestern Guizhou Province. Engine Industry Press, Beijing (in Chinese)

Large RR, Danyushevsky L, Hollit C, Maslennikov V, Meffre S, Gilbert S, Bull S, Scott R, Emsbo P, Thomas H (2009) Gold and trace element zonation in pyrite using a laser imaging technique: implications for the timing of gold in orogenic and Carlin-style sediment-hosted deposits. Econ Geol 104:635–668

Li Z, Ye L, Huang Z, Nian H, Zhou J (2016) Primary research on trace elements in sphalerite from Tianqiao Pb-Zn deposit, northwestern Guizhou Province, China. Acta Mineral Sin 36:183–188 (**(in Chinese with English abstract)**)

Li Z, Ye L, Hu Y, Wei C, Huang Z, Yang Y, Danyushevsky L (2020) Trace elements in sulfides from the Maozu Pb-Zn deposit, Yunnan Province, China: Implications for trace-element incorporation mechanisms and ore genesis. Am Mineral 105:1734–1751

Liu HC, Lin WD (1999) Study on the law of Pb-Zn-Ag ore deposit in Northeast Yunnan. Yunann University Press, Kunming (in Chinese), China

Liu Y, Hu Z, Gao S, Günther D, Xu J, Gao C, Chen H (2008) *In-situ* analysis of major and trace elements of anhydrous minerals by LA-ICP-MS without applying an internal standard. Chem Geol 257:34–43

Mao D, He J, Liao C (2001) Sedimentary-reformation metallogenic characteristics of the Tianqiao Lead-Zinc deposit. Geol Geochem 29:21–27 (**(in Chinese with English abstract)**)

Meng Y-M, Qi H-W, Hu R-Z (2015) Determination of germanium isotopic compositions of sulfides by hydride generation MC-ICP-MS and its application to the Pb–Zn deposits in SW China. Ore Geol Rev 65:1095–1109

Meng Y-M, Hu R-Z, Huang X-W, Gao J-F, Qi L, Lyu C (2018) The relationship between stratabound Pb-Zn-Ag and porphyry-skarn Mo mineralization in the Laochang deposit, southwestern China: Constraints from pyrite Re-Os isotope, sulfur isotope, and trace element data. J Geochem Explor 194:218–238

Meng YM, Hu RZ, Huang XW, Gao JF, Sasseville C (2019) The origin of the carbonate-hosted Huize Zn–Pb–Ag deposit, Yunnan province, SW China: constraints from the trace element and sulfur isotopic compositions of pyrite. Mineral Petrol 113:369–391

Meng YM (2014) Application of Ge isotopes to mineral deposits: examples from the Wulantuga Ge deposit of Inner Mongolia, the Huize and other Pb-Zn deposits of SW China. Unpublished PhD thesis, Institute of Geochemistry, Chinese Academy of Sciences

Mukherjee I, Large R (2017) Application of pyrite trace element chemistry to exploration for SEDEX style Zn–Pb deposits: McArthur Basin, Northern Territory, Australia. Ore Geol Rev 81:1249–1270

Qiu YM, Gao S, McNaughton NJ, Groves DI, Ling W (2000) First evidence of > 3.2 Ga continental crust in the Yangtze craton of south China and its implications for Archean crustal evolution and Phanerozoic tectonics. Geology 28:11–14

Reich M, Deditius A, Chryssoulis S, Li J-W, Ma C-Q, Parada MA, Barra F, Mittermayr F (2013) Pyrite as a record of hydrothermal fluid evolution in a porphyry copper system: A SIMS/EMPA trace element study. Geochim Cosmochim Acta 104:42–62

Reich M, Simon AC, Deditius A, Barra F, Chryssoulis S, Lagas G, Tardani D, Knipping J, Bilenker L, Sánchez-Alfaro P (2016) Trace element signature of pyrite from the Los Colorados iron oxide-apatite (IOA) deposit, Chile: a missing link between Andean IOA and iron oxide copper-old systems? Econ Geol 111:743–761

Sun W-H, Zhou M-F, Gao J-F, Yang Y-H, Zhao X-F, Zhao J-H (2009) Detrital zircon U-Pb geochronological and Lu–Hf isotopic constraints on the Precambrian magmatic and crustal evolution of the western Yangtze Block, SW China. Precambrian Res 172:99–126

Tanner D, Henley RW, Mavrogenes JA, Holden P (2016) Sulfur isotope and trace element systematics of zoned pyrite crystals from the El Indio Au–Cu–Ag deposit. Chile Contrib Mineral Petrol 171:33

Ward J, Mavrogenes J, Murray A, Holden P (2017) Trace element and sulfur isotopic evidence for redox changes during formation of the Wallaby Gold Deposit, Western Australia. Ore Geol Rev 82:31–48

Yan D-P, Zhou M-F, Song H-L, Wang X-W, Malpas J (2003) Origin and tectonic significance of a Mesozoic multi-layer over-thrust system within the Yangtze Block (South China). Tectonophysics 361:239–254

Zhang C, Wu Y, Hou L, Mao J (2015) Geodynamic setting of mineralization of Mississippi Valley-type deposits in world-class Sichuan–Yunnan–Guizhou Zn–Pb triangle, southwest China: Implications from age-dating studies in the past decade and the Sm–Nd age of Jinshachang deposit. J Asian Earth Sci 103:103–114

Zhang Y, Han R-S, Ding X, Wang Y-R, Wei P-T (2019) Experimental study on fluid migration mechanism related to Pb–Zn super-enrichment: Implications for mineralisation mechanisms of the Pb–Zn deposits in the Sichuan–Yunnan–Guizhou SW China. Ore Geol Rev 114:103110

Zhao J-H, Zhou M-F, Yan D-P, Zheng J-P, Li J-W (2011) Reappraisal of the ages of Neoproterozoic strata in South China: no connection with the Grenvillian orogeny. Geology 39:299–302

Zhou M-F, Yan D-P, Kennedy AK, Li Y, Ding JJE, Letters PS (2002) SHRIMP U-Pb zircon geochronological and geochemical evidence for Neoproterozoic arc-magmatism along the western margin of the Yangtze Block, South China. Earth Planet Sci Lett 196:51–67

Zhou M-F, Arndt NT, Malpas J, Wang CY, Kennedy AK (2008) Two magma series and associated ore deposit types in the Permian Emeishan large igneous province, SW China. Lithos 103:352–368

Zhou J, Huang Z, Zhou G, Li X, Ding W, Bao G (2010) Sulfur isotopic composition of the Tianqiao Pb-Zn ore deposit, Northwest Guizhou Province, China: Implications for the source of sulfur in the ore-forming fluids. Chin J Geochem 29:301–306

Zhou J, Huang Z, Zhou G, Li X, Ding W, Bao G (2011) Trace Elements and Rare Earth Elements of Sulfide Minerals in the Tianqiao Pb-Zn Ore Deposit, Guizhou Province, China. Acta Geol Sin 85:189–199

Zhou J, Huang Z, Zhou M, Li X, Jin Z (2013) Constraints of C-O–S–Pb isotope compositions and Rb–Sr isotopic age on the origin of

the Tianqiao carbonate-hosted Pb–Zn deposit, SW China. Ore Geol Rev 53:77–92

Zhou J-X, Huang Z-L, Zhou M-F, Zhu X-K, Muchez P (2014) Zinc, sulfur and lead isotopic variations in carbonate-hosted Pb–Zn sulfide deposits, southwest China. Ore Geol Rev 58:41–54

Zhou J-X, Xiang Z-Z, Zhou M-F, Feng Y-X, Luo K, Huang Z-L, Wu T (2018) The giant Upper Yangtze Pb–Zn province in SW China: Reviews, new advances and a new genetic model. J Asian Earth Sci 154:280–315